

A first extraction of gluon TMDs from Higgs data at the LHC

The **MAP** (Multi-dimensional Analysis of Partonic distributions) Collaboration

Simone Anedda,^{1,2,*} Valerio Bertone,^{3,†} Giuseppe Bozzi,^{1,2,‡} and Matteo Cerutti^{3,§}

¹*Dipartimento di Fisica, Università di Cagliari, Cittadella Universitaria, I-09042 Monserrato (CA), Italy*

²*INFN - Sezione di Cagliari, Cittadella Universitaria, I-09042 Monserrato (CA), Italy*

³*Université Paris-Saclay - CEA - IRFU, 91191 Gif-sur-Yvette, France*

We present the first extraction of the unpolarised gluon transverse-momentum-dependent (TMD) parton distribution from Higgs-boson production data at the LHC within the framework of TMD factorisation. The analysis is based on the currently available set of ATLAS and CMS measurements of the Higgs q_T distribution at $\sqrt{s} = 8$ and 13 TeV in the diphoton and four-lepton decay channels, restricted to the small- q_T region where TMD factorisation is applicable. Theoretical predictions are computed up to N³LL accuracy, with the contribution of the linearly polarised gluon TMD $h_1^{\perp g}$ accounted for. Fiducial selections are consistently incorporated for both two- (diphoton) and four-body (four-lepton) final states. The fit reproduces both the shape and the normalisation of the experimental data, and yields a moderate sensitivity to the nonperturbative content of gluon TMDs. We further assess the convergence of the perturbative expansion and the stability of the extracted distribution under variations of the q_T cut. This analysis provides a baseline for future extractions combining LHC Higgs measurements with other gluon-sensitive processes spanning a broader range of hard scales.

I. INTRODUCTION

The internal structure of the proton is described, at leading power in the hard scale, by parton distribution functions (PDFs). When the transverse momentum of partons with respect to the proton direction of motion is resolved, this description is extended to transverse-momentum dependent distributions (TMDs), which encode both the longitudinal momentum fraction x and the intrinsic transverse momentum \mathbf{k}_\perp of partons inside a fast-moving hadron. TMD factorisation theorems [1, 2] allow us to express the differential cross section for suitable processes characterised by an inclusive final state with invariant mass Q and transverse momentum $q_T \equiv |\mathbf{q}_T| \ll Q$ as convolutions of TMD distributions with perturbatively calculable hard coefficients. Importantly, TMDs obey specific evolution equations whose solution gives rise to the characteristic resummation of large logarithms $\ln(Q^2/q_T^2)$.

Whereas quark TMDs have been extensively studied and extracted from Drell-Yan and semi-inclusive deep-inelastic scattering data over the past two decades [3–12], gluon TMDs remain far less constrained. This asymmetry can mostly be ascribed to the scarcity of experimental information. As a matter of fact, a clean extraction of the unpolarised gluon TMDs requires processes whose final state is colour-singlet, so that soft and collinear radiation factorises without ambiguity [13–15]. Conversely, colour-entanglement issues can compromise TMD factorisation in processes with coloured final states such as jets or quarkonia. Nonetheless, a broad literature exists which includes studies of the gluon TMDs such as quarkonium production at the LHC [16, 17], gluon linear-polarisation effects [18–22], and model calculations [23, 24].

Inclusive Higgs production in proton-proton collisions is possibly the cleanest probe of the unpolarised gluon TMDs. Indeed, at the LHC the Higgs boson is predominantly produced through gluon fusion. Taking into account only electroweak decay modes, the observed colour-singlet final state avoids colour-entanglement issues that could hamper TMD factorisation.

The theoretical description of the Higgs q_T distribution has a long history. At small q_T , the resummation of large logarithms of q_T is necessary to obtain reliable perturbative predictions. The groundwork for such resummation in the b -space formalism was laid by Collins, Soper and Sterman (CSS) [1], and the Higgs case was first worked out explicitly at next-to-leading logarithmic (NLL) accuracy in Refs. [25, 26]. A comprehensive framework combining resummation at small q_T with fixed-order matching at large q_T was developed in Ref. [15], who computed the Higgs q_T distribution at next-to-next-to-leading logarithmic (NNLL) accuracy matched to next-to-leading order (NLO).

*Electronic address: sanedda@dsf.unica.it –ORCID: 0009-0005-4921-2850

†Electronic address: valerio.bertone@cea.fr – ORCID: 0000-0003-0148-0272

‡Electronic address: giuseppe.bozzi@unica.it – ORCID: 0000-0002-2908-6077

§Electronic address: matteo.cerutti@cea.fr –ORCID: 0000-0001-7238-5657

Subsequent advances pushed the accuracy to N³LL+NNLO, achieved with different methods, such as momentum-space resummation in Ref. [27], and soft-collinear effective theory (SCET) in Ref. [28]. These developments established the theoretical infrastructure required for precision phenomenology of the Higgs q_T distribution.

In the small- q_T region, the differential Higgs cross section becomes directly sensitive to the unpolarised gluon TMD f_1^g and to the linearly polarised gluon TMD $h_1^{\perp g}$ (Boer-Mulders function). The linearly polarised gluon TMD was first studied in Ref. [29], where it was shown that an unpolarised hadron can contain gluons with linear polarisation in the transverse plane, giving rise to an independent TMD that contributes to the cross section on equal footing with f_1^g . The matching of $h_1^{\perp g}$ onto collinear gluon PDFs was computed at NLO in Refs. [30, 31] and pushed to NNLO in Ref. [32], completing the perturbative ingredients needed for a consistent NNLO treatment of both gluon TMDs in Higgs production.

Despite this theoretical progress, a direct extraction of gluon TMDs from experimental data remains an open challenge. The reason is partly experimental: precision measurements of the Higgs q_T distribution have only recently become available from the ATLAS and CMS experiments at Run I and Run II of the LHC, covering both the di-photon and four-lepton decay channels. These datasets, while limited in statistical power, now constitute a viable basis for a first phenomenological extraction.

In this paper, we present the first extraction of the unpolarised gluon TMD f_1^g from LHC Higgs data within the TMD factorisation framework, employing perturbative accuracy up to N³LL. We consider the complete set of available ATLAS and CMS measurements of the Higgs q_T distribution in the $H \rightarrow \gamma\gamma$ and $H \rightarrow 4\ell$ decay channels, and perform a fit using the NangaParbat framework [7] developed by the MAP Collaboration. We assess the quality of the fit, the nonperturbative sensitivity of the current dataset, and the convergence of the perturbative series from NLL' to N³LL. The linearly polarised gluon contribution is included in the theoretical predictions with its NNLO matching coefficient, and its numerical impact on the extracted distributions is discussed.

The paper is organised as follows: section II provides an overview of the TMD formalism used in the analysis; section III describes the datasets considered in the fitting procedure and discusses the implementation of the selection cuts in our theoretical framework; section IV presents the numerical results of the fit and the k_T shape of the extracted gluon TMD; in section V we draw our conclusions and elaborate on possible extensions of the present work.

II. FORMALISM

We consider the following process

$$p(P_1) + p(P_2) \rightarrow H(q) + X, \quad (1)$$

in which two protons with four-momenta P_1 and P_2 , such that $(P_1 + P_2)^2 = s$, collide to inclusively produce an on-shell Higgs boson of invariant mass $\sqrt{q^2} = M_H = 125.1$ GeV, rapidity y , and transverse momentum \mathbf{q}_T .

The dominant partonic production channel at the LHC is gluon fusion, $gg \rightarrow H$, mediated at leading order by a heavy quark loop, as illustrated in Fig. 1. Since the Yukawa coupling of the Higgs boson to fermions is proportional to the fermion mass, the amplitude is dominated by a virtual top loop, and contributions from lighter quarks (e.g. b, c) can be neglected.

The LO matrix element squared for Higgs production in gluon fusion is [33]

$$|M(gg \rightarrow H)|^2 = \frac{\alpha_s^2(M_H) M_H^4 G_F}{288\pi\sqrt{2}} \left| A_Q \left(\frac{4M_t^2}{M_H^2} \right) \right|^2, \quad (2)$$

where $\alpha_s(M_H)$ is the strong coupling evaluated at the Higgs mass, $G_F = 1.16639 \times 10^{-5}$ GeV⁻² is the Fermi constant, and $M_t = 172.9$ GeV denotes the on-shell pole mass of the top. The function A_Q is given by

$$A_Q(x) = \frac{3}{2} x \left[1 + (1-x)f(x) \right],$$

$$f(x) = \begin{cases} \arcsin^2\left(\frac{1}{\sqrt{x}}\right), & x \geq 1, \\ -\frac{1}{4} \left[\ln\left(\frac{1+\sqrt{1-x}}{1-\sqrt{1-x}}\right) - i\pi \right]^2, & x < 1. \end{cases} \quad (3)$$

In the small transverse momentum region, $q_T \ll M_H$ with $q_T = |\mathbf{q}_T|$, the differential cross section for the production of an Higgs boson can be factorised in terms of TMDs. Moreover, we use the narrow-width approximation (NWA)

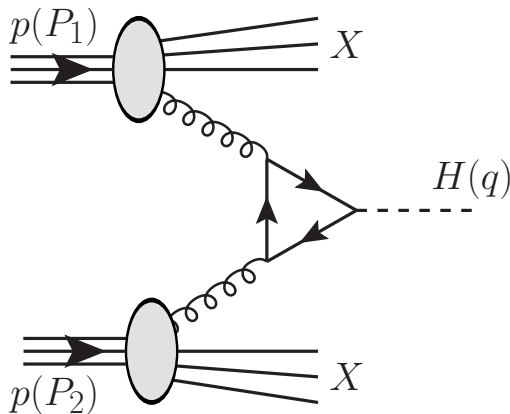


FIG. 1: Higgs production in pp collisions through gluon fusion at leading order.

which sets the Higgs on the mass shell, producing

$$\frac{d\sigma}{dydq_T^2} = \mathcal{P}(M_H, y, q_T) \frac{\alpha_s^2(M_H) G_F}{288\pi\sqrt{2}} H_{ggH}(M_H, \mu) \int_0^\infty db_T b_T J_0(q_T b_T) \times \left[f_1^g(x_1, b_T; \mu, \zeta_1) f_1^g(x_2, b_T; \mu, \zeta_2) + h_1^{\perp g}(x_1, b_T; \mu, \zeta_1) h_1^{\perp g}(x_2, b_T; \mu, \zeta_2) \right], \quad (4)$$

where $x_{1,2} = (M_H/\sqrt{s})e^{\pm y}$ are the light-cone momentum fractions. \mathcal{P} is the phase-space reduction factor associated with the kinematic cuts on the final state which will be discussed in section III. The perturbative hard function H_{ggH} embodies hard and virtual contributions to the cross section and its perturbative coefficients up to $\mathcal{O}(\alpha_s^2)$ can be found in Ref. [27]. The unpolarised and linearly polarised (Boer-Mulders) TMDs f_1^g and $h_1^{\perp g}$, respectively, are expressed in \mathbf{b}_T space (with $b_T \equiv |\mathbf{b}_T|$) Fourier-conjugate to \mathbf{q}_T . Finally, the renormalisation scale μ and the two rapidity scales ζ_1 and ζ_2 are set as follows: $\mu^2 = \zeta_1 = \zeta_2 = M_H^2$.

As is well known, for small values of b_T both TMDs f_1^g and $h_1^{\perp g}$ can be matched on the unpolarised collinear PDFs. Specifically, one has:

$$f_1^g(x, b_T; \mu_b, \mu_b^2) = \sum_{i=g,q} \int_x^1 \frac{dy}{y} C_{gi}(y, \alpha_s(\mu_b)) f_i\left(\frac{x}{y}, \mu_b\right) \equiv [C \otimes f]_g(x, b_T; \mu_b, \mu_b^2), \quad (5)$$

$$h_1^{\perp g}(x, b_T; \mu_b, \mu_b^2) = \sum_{i=g,q} \int_x^1 \frac{dy}{y} G_{gi}(y, \alpha_s(\mu_b)) f_i\left(\frac{x}{y}, \mu_b\right) \equiv [G \otimes f]_g(x, b_T; \mu_b, \mu_b^2),$$

where $\mu_b = 2e^{-\gamma_E}/b_T$, with γ_E the Euler-Mascheroni constant, and f_i correspond to the unpolarised collinear PDFs, which are taken from the NNPDF3.1 set [34] with perturbative charm at the appropriate perturbative order [6] and accessed through the LHAPDF library [35]. Also the running of the strong coupling α_s is taken from the PDF set. The matching functions C_{gi} and G_{gi} admit the following perturbative expansions:

$$C_{gi}(y, \alpha_s) = \delta(1-y) + \sum_{n=1}^{\infty} \left(\frac{\alpha_s}{4\pi}\right)^n C_{gi}^{[n]}(y), \quad (6)$$

$$G_{gi}(y, \alpha_s) = \sum_{n=1}^{\infty} \left(\frac{\alpha_s}{4\pi}\right)^n G_{gi}^{[n]}(y),$$

which we truncate at $\mathcal{O}(\alpha_s)$ for NLL' and NNLL, and at $\mathcal{O}(\alpha_s^2)$ for NNLL' and N³LL. Moreover, TMDs obey evolution equations that govern their dependence on μ and ζ . The solution to these evolution equations is encoded in the so-called Sudakov form factor, which is the same for both unpolarised and linearly-polarised gluon TMDs and reads

$$R^g[(\mu_b, \mu_b^2) \rightarrow (\mu, \zeta)] = \exp \left\{ K^g(\mu_b) \ln \frac{\sqrt{\zeta}}{\mu_b} + \int_{\mu_b}^{\mu} \frac{d\mu'}{\mu'} \left[\gamma_F^g(\alpha_s(\mu')) - \gamma_K^g(\alpha_s(\mu')) \ln \frac{\sqrt{\zeta}}{\mu'} \right] \right\}. \quad (7)$$

The gluon anomalous dimensions K^g (Collins-Soper), γ_F^g (non-cusp), and γ_K^g (cusp) also admit a perturbative expansion and are truncated at the appropriate order depending on whether the cross-section computation is carried out at NLL', NNLL, NNLL', or N³LL [6].

Finally, TMDs can be computed as follows:

$$\begin{aligned} f_1^g(x, b_T; \mu, \zeta) &= R^g [(\mu_b, \mu_b^2) \rightarrow (\mu, \zeta)] [C \otimes f]_g(x, b_T; \mu_b, \mu_b^2), \\ h_1^{\perp g}(x, b_T; \mu, \zeta) &= R^g [(\mu_b, \mu_b^2) \rightarrow (\mu, \zeta)] [G \otimes f]_g(x, b_T; \mu_b, \mu_b^2). \end{aligned} \quad (8)$$

However, when b_T becomes large, or equivalently when μ_b becomes small, these expressions become unreliable because of the onset of nonperturbative effects. Indeed, in this region the strong coupling approaches the Landau pole and the matching formulas in Eq. (5) receive large power corrections. In order to account for nonperturbative effects, we follow the traditional CSS strategy [1] by introducing the function [3]

$$b_*(b_T) = b_{\max} \left(\frac{1 - e^{-b_T^4/b_{\max}^4}}{1 - e^{-b_T^4/b_{\min}^4}} \right)^{1/4}, \quad (9)$$

with $b_{\max} = 2e^{-\gamma_E}$ and $b_{\min} = 2e^{-\gamma_E}/M_H$, and rewriting the TMDs as follows:

$$\begin{aligned} f_1^g(x, b_T; \mu, \zeta) &\rightarrow f_1^g(x, b_*(b_T); \mu, \zeta) f_{\text{NP}}(x, b_T, \zeta), \\ h_1^{\perp g}(x, b_T; \mu, \zeta) &\rightarrow h_1^{\perp g}(x, b_*(b_T); \mu, \zeta) f_{\text{NP}}(x, b_T, \zeta). \end{aligned} \quad (10)$$

Since $b_*(b_T)$ never becomes too large even for large values of b_T , the replacements above guarantee that TMDs computed in $b_*(b_T)$ are always in a regime where perturbative matching and evolution are accurate. Nonperturbative effects are instead factored out into the function f_{NP} , which needs to be parametrised and fitted to data (for more details see, *e.g.*, Refs. [6, 36]). In this study, we choose a simple Gaussian parametrisation:

$$f_{\text{NP}}(x, b_T, \zeta) = \exp \left[-\frac{1}{2} g b_T^2 \right], \quad (11)$$

with g a free parameter to be determined from data. Two observations are in order. The first is that f_{NP} is assumed to be the same for both unpolarised and linearly-polarised TMDs. In general, this might not be the case. However, current data does not allow to determine f_{NP} separately for the two TMDs involved in the calculation. The second observation is that, in general, f_{NP} is also a function of the rapidity scale ζ . In fact, the ζ dependence of f_{NP} determines the non perturbative contribution to the Collins-Soper kernel (see, *e.g.*, Ref. [12]). However, within the NWA, data are considered at one single scale, *i.e.* $\zeta = M_H^2$. As a consequence, we have no way to determine the ζ dependence of f_{NP} . Therefore, Eq. (11) is to be considered valid only at $\zeta = M_H^2$.

III. EXPERIMENTAL DATA

In this section we describe the experimental datasets included in our analysis. We consider measurements of the Higgs-boson transverse-momentum (q_T) distribution performed by the ATLAS and CMS experiments in the diphoton ($\gamma\gamma$) and four-lepton (4ℓ) decay channels. The breakdown of the full dataset included in this analysis is summarised in Table I.

The datasets considered span different center-of-mass energies ($\sqrt{s} = 8$ and 13 TeV) and probe phase-space regions characterised by an invariant mass of the Higgs boson around its on-shell mass M_H and typical momentum fractions $x \sim 10^{-2}$. As for the ATLAS measurements, we include only combined results when available, in order to avoid double counting. Since the analysis is performed within the NWA, the experimental data provides information only at a single hard scale, M_H . Also, the included datasets are integrated in rapidity y and thus provide very little sensitivity to the x dependence of TMDs.

Our analysis is restricted to the region of validity of TMD factorisation (Eq. (4)). As a consequence, we need to require an upper value on the value of q_T of the data points included in the analysis. As a baseline, we choose to cut all data points which do not respect the cut $q_T/M_H < 0.3$. However, we also consider two more conservative cuts, namely $q_T/M_H < 0.25$ and $q_T/M_H < 0.2$. Since measurements are provided in finite transverse-momentum bins, the cut is conservatively applied using the upper edge of each q_T bin. The numbers of data points satisfying the q_T -cut conditions for all of the choices discussed above are reported in Table I for the single datasets and for the full ensemble. With the baseline cut ($q_T/M_H < 0.3$), we include in the fit a total of 30 points.

Dataset	N_{dat}			Decay channel	\sqrt{s} [GeV]	Ref.
	$q_T/M_H < 0.2$	$q_T/M_H < 0.25$	$q_T/M_H < 0.3$			
CMS Run II (2017–2018)	5	6	7	$H \rightarrow \gamma\gamma$	13000	[37]
CMS Run II (2017–2018)	2	3	3	$H \rightarrow 4\ell$	13000	[38]
CMS Run II (2015–2016)	1	2	2	combined	13000	[39]
CMS Run I	1	2	2	$H \rightarrow \gamma\gamma$	800	[40]
ATLAS Run II (2017–2018)	5	6	7	$H \rightarrow \gamma\gamma$	13000	[41]
ATLAS Run II (2017–2018)	2	3	3	$H \rightarrow 4\ell$	13000	[42]
ATLAS Run II (2015–2016)	2	3	3	combined	13000	[43]
ATLAS Run I	1	2	2	$H \rightarrow \gamma\gamma$	800	[44]
ATLAS Run I	1	1	1	$H \rightarrow 4\ell$	800	[45]
Total	20	28	30	–	–	–

TABLE I: Breakdown of the datasets included in this analysis. For each dataset, the table includes information on: the number of data points (N_{dat}) passing three different cuts in q_T/M_H , the Higgs-boson decay channel, the center-of-mass energy \sqrt{s} , and the reference.

All measurements are defined within fiducial phase-space regions, characterised by kinematic cuts on final-state leptons or photons. These effects are accounted for in the theory predictions through the phase-space reduction factor \mathcal{P} (see Eq. (4) and Appendix A). Combined measurements, which are extrapolated to the full phase space, are treated accordingly without fiducial cuts. Tables II-III summarise the fiducial cuts implemented for each channel and experiment.

Dataset	$p_{T,\ell}$ [GeV]	$ \eta_\ell $	Event p_T [GeV]	$m_{\ell\ell}$ [GeV]
CMS Run II (2017–2018)	$> 7 (e), > 5 (\mu)$	$< 2.5 (e), < 2.4 (\mu)$	$> 20, > 10$	$40 < m_{12} < 120, 12 < m_{34} < 120$
ATLAS Run I	$> 7 (e), > 6 (\mu)$	$< 2.47 (e), < 2.7 (\mu)$	$> 20, > 15, > 10$	$50 < m_{12} < 106, 12 < m_{34} < 115$
ATLAS Run II (2017–2018)	$> 7 (e), > 5 (\mu)$	$< 2.47 (e), < 2.7 (\mu)$	$> 20, > 15, > 10$	$50 < m_{12} < 106, 12 < m_{34} < 115$

TABLE II: Fiducial selection requirements for the $H \rightarrow 4\ell$ channel.

Dataset	$p_{T,\gamma_1}/m_{\gamma\gamma}$	$p_{T,\gamma_2}/m_{\gamma\gamma}$	$ \eta_\gamma $
CMS Run II (2017–2018)	> 0.35	> 0.25	$ \eta_\gamma < 1.4442 \vee 1.566 < \eta_\gamma < 2.5$
CMS Run I	> 0.35	> 0.25	$ \eta_\gamma < 1.44 \vee 1.57 < \eta_\gamma < 2.5$
ATLAS Run I	> 0.35	> 0.25	$ \eta_\gamma < 1.37 \vee 1.56 < \eta_\gamma < 2.37$
ATLAS Run II (2017–2018)	> 0.35	> 0.25	$ \eta_\gamma < 1.37 \vee 1.52 < \eta_\gamma < 2.37$

TABLE III: Fiducial selection requirements for the $H \rightarrow \gamma\gamma$ channel.

Experimental uncertainties include both uncorrelated and correlated components which are fully incorporated in our analysis following the treatment adopted in past TMD analyses, (*e.g.* see Refs. [6, 7, 10, 12, 46–49]). The collinear PDF set used in the computation of TMDs (NNPDF3.1 [34], in our case) carries additional uncertainties, which in principle should be accounted for. However, we found that PDF uncertainties are at least one order of magnitude smaller than the experimental ones. Therefore, we decided not to include them.

We finally stress that no other normalisation factors have been applied in this analysis, with the consequence that both shape and normalisation of the experimental measurements have an impact on the fit.

IV. RESULTS

In this section, we present the results of the extraction of unpolarised gluon TMDs from the current available measurements of Higgs production (see Sec. III). In Sec. IV A, we discuss the quality of the fit at N³LL in terms of theory/data agreement. In Sec. IV B, we present the extracted gluon TMDs from our analysis. In Sec. IV C, we discuss the convergence of perturbative corrections. Finally, in Sec. IV D, we study the dependence of the fit results on the q_T cut.

A. Fit quality

In this section, we present the quality of the baseline fit at N³LL with cut $q_T/M_H < 0.3$. The error analysis makes use of the bootstrap method, namely by fitting an ensemble of $N_{\text{rep}} = 200$ of Monte Carlo replicas of the experimental data. Although the most complete statistical information is represented by the full ensemble of replicas, we choose the χ^2 of the central replica, representing the best fit to the unfluctuated data, as the best estimator of fit quality.

Tab. IV shows the breakdown of χ^2 's normalised to the number N_{dat} of data points for each of the included measurements and for the full dataset. We note that the value of the global $\chi^2/N_{\text{dat}} = 1.49$, corresponding to a p -value of about 3%, indicates that the fit is able to reasonably reproduce the overall shape and normalisation of the datasets. Some residual tension is observed, which can be attributed to statistical fluctuations in the region of relatively large q_T . This tension can be significantly reduced by adopting a more conservative cut in q_T/M_H (see Sec. IV D for details).

Dataset	N_{dat}	χ^2/N_{dat}
CMS Run II $H \rightarrow \gamma\gamma$	7	1.15
CMS Run II $H \rightarrow 4\ell$	3	1.17
CMS Run II (combined)	2	4.46
CMS Run I $H \rightarrow \gamma\gamma$	2	0.26
ATLAS Run II $H \rightarrow \gamma\gamma$	7	1.52
ATLAS Run II $H \rightarrow 4\ell$	3	0.93
ATLAS Run II (combined)	3	0.99
ATLAS Run I $H \rightarrow \gamma\gamma$	2	3.58
ATLAS Run I $H \rightarrow 4\ell$	1	0.004
Total	30	1.49

TABLE IV: Breakdown of the normalised χ^2 to the number of data points N_{dat} of the central replica for each dataset included in the fit.

Concerning the individual experiments, we observe that the description of the $H \rightarrow \gamma\gamma$ measurements is generally worse than for the rest of the dataset. In particular, the CMS Run II (combined) and ATLAS Run I $H \rightarrow \gamma\gamma$ data exhibit the largest deviations from the fitted theoretical predictions, and determine a significant increase of the global χ^2 .

In order to visualize the quality of our fit, we present in Fig. 2 the comparison between experimental data and theoretical results for a representative selection of datasets. We display in the upper panel of each plot the q_T -differential cross section, and in the lower panel the data-to-theory ratio. Coloured bands represent one-sigma uncertainties.

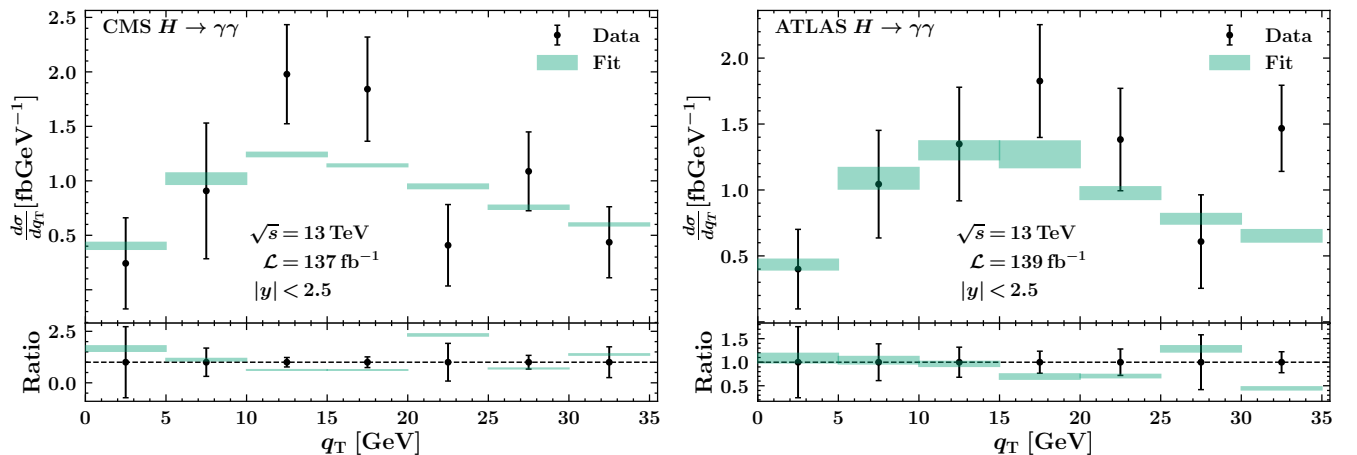


FIG. 2: Upper panels: comparison between experimental data and theoretical predictions for the q_T -differential cross section for Higgs production measurements from CMS Run II (left panel) and ATLAS Run II (right panel); uncertainty bands correspond to one-sigma error. Lower panel: ratio between experimental data and theoretical results.

We find that theoretical predictions are able to reproduce both shape and normalisation of data. Some tension

is observed in the peak region of CMS Run II $H \rightarrow \gamma\gamma$ data and in the tail of the ATLAS Run II $H \rightarrow \gamma\gamma$ data. However, as we will prove below, this tension can be significantly reduced by adopting a more conservative q_T cut. Note that the larger theoretical uncertainty bands in the right panel are due to the effect of the systematic shifts induced by correlated experimental errors, which are particularly relevant for the ATLAS Run II $H \rightarrow \gamma\gamma$ dataset.

B. Extracted gluon TMDs

Now we move on to presenting the gluon unpolarised TMD distribution f_1^g extracted from our baseline fit at N³LL with kinematic cut $q_T/M_H < 0.3$.¹ In order to gauge the sensitivity of the included experimental data on the intrinsic nonperturbative part of TMDs, we report the value of the free parameter g obtained from the fit:

$$g = 15.6 \pm 5.1 \text{ GeV}^2, \quad (12)$$

which corresponds to average and standard deviation over the set of 200 Monte Carlo replicas. We observe that the parameter is determined with a relative uncertainty of about 35%, which indicates that the current dataset has moderate sensitivity to the nonperturbative part of TMDs. This is consistent with the fact that the included measurements cover a kinematic region at very large scale, where the perturbative contribution to TMDs is dominant. In Sec. IV D, we will explore the effect on the parameter g of adopting more conservative cuts in q_T .

As mentioned above, the NWA prevents the possibility of disentangling the nonperturbative contribution of the Collins-Soper kernel, related to gluon TMD evolution, from the rest of the nonperturbative effects, which we will refer to as intrinsic component. In order to achieve this separation, it is necessary to include measurements spanning different scales broadly different from M_H , such as J/ψ production data. We leave this to a future work. Nevertheless, it is instructive to perform an *a posteriori* decomposition, by identifying

$$g = g_1 + g_2^g \log(\zeta/Q_0^2), \quad (13)$$

with $Q_0 = 1 \text{ GeV}$ and where g_1 represents the intrinsic component and g_2^g the nonperturbative evolution. We estimate g_2^g from the quark value extracted in Ref. [50], $g_2 = 0.167 \pm 0.015 \text{ GeV}^2$, rescaled by a factor C_A/C_F . This assumption is motivated by perturbative considerations and provides a natural guess in the absence of direct constraints.

We propagate uncertainties via bootstrap sampling of 10^5 replicas of (g, g_2^g) obtaining

$$g_1 = 14.4 \pm 5.1 \text{ GeV}^2, \quad (14)$$

which allows us to calculate gluon TMDs at values of $\mu = \sqrt{\zeta} = Q$ different from M_H . We note that the value of g_1 is close to the total g , indicating that, within the current kinematic coverage, the nonperturbative evolution contribution is small. This confirms the current limited sensitivity of Higgs measurements on nonperturbative TMD effects.

In Fig. 3, we show the unpolarised TMD gluon PDF as a function of the intrinsic transverse momentum $|\mathbf{k}_\perp|$. In the left panel, we show the TMD PDFs at the nominal scales $\mu = \sqrt{\zeta} = M_H$ for different values of x , namely $x = 0.001, 0.01, 0.1$. In the right panel, we show the TMD PDF at $x = 0.01$ at three different values of $Q = \mu = \sqrt{\zeta}$, specifically $Q = 6 \text{ GeV}$, which roughly corresponds to the production of a pair of J/ψ 's, the usual M_H , and $Q = 350 \text{ GeV}$, which is the typical energy for the production of a $t\bar{t}$ pair. Bands correspond to one-sigma uncertainties.

We observe the gluon TMD grows in size as x decreases. In fact, its $|\mathbf{k}_\perp|$ -integral is related to the gluon collinear PDFs, which indeed grows very rapidly at large scales and small values of x . We also stress that the behaviour in x of the gluon TMD is fully driven by the perturbative matching and collinear PDFs because our model for f_{NP} is independent of x . Finally, we observe that the gluon TMD becomes broader at larger values of Q as a consequence of the evolution.

C. Perturbative convergence

In previous sections we discussed our baseline fit, which was obtained at N³LL accuracy. We now show the importance of including higher-order perturbative corrections in the theoretical predictions to achieve a good description of the experimental data. To this end, we perform additional fits at lower perturbative accuracy, namely at NLL',

¹ Also the linearly polarised gluon TMD $h_1^{\perp g}$ is accounted for in this analysis. However, data is little sensitive to this TMD, so we do not find it particularly instructive to discuss it here and draw any conclusions.

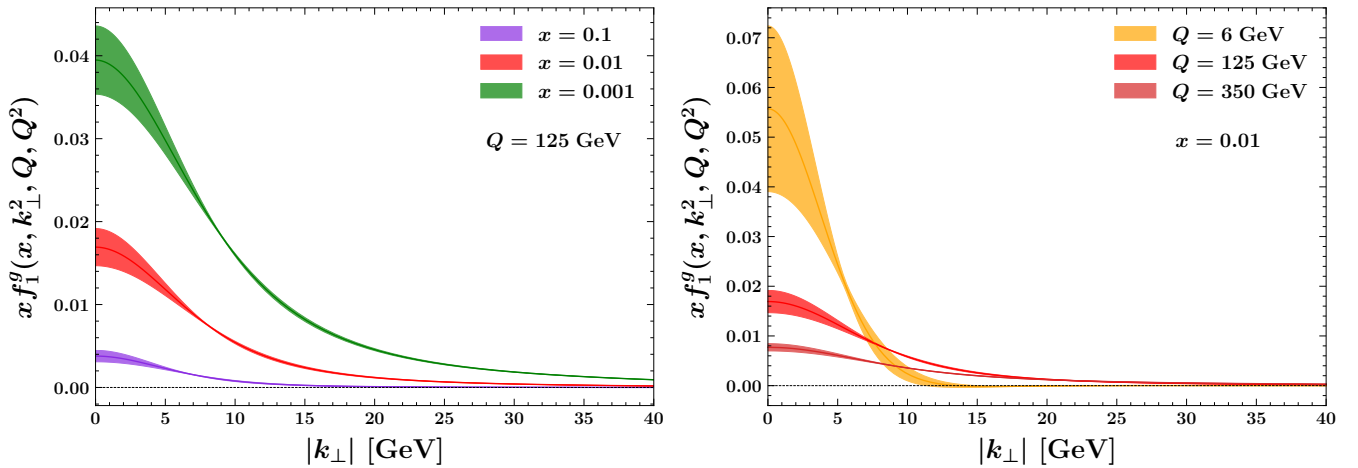


FIG. 3: Left panel: The TMD PDF of the gluon in a proton at $\mu = \sqrt{\zeta} = 125$ GeV as a function of the partonic transverse momentum $|k_\perp|$ for $x = 0.001, 0.01, 0.1$. Right panel: gluon TMD PDF at $x = 0.01$ for $\mu = \sqrt{\zeta} = 6, 125, 350$ GeV. Uncertainty bands correspond to one-sigma error.

NNLL, and NNLL' [6], and compare the results with the baseline N³LL fit. We do not consider LL and NLL accuracies because in both cases the data/theory agreement is very poor. For these additional fits, we use the baseline cut $q_T/M_H < 0.3$.

In Fig. 4, we show the behaviour of the global χ^2 as the perturbative accuracy increases. Note that we didn't divide for the number N_{dat} of data points in order to better appreciate the size of the differences.

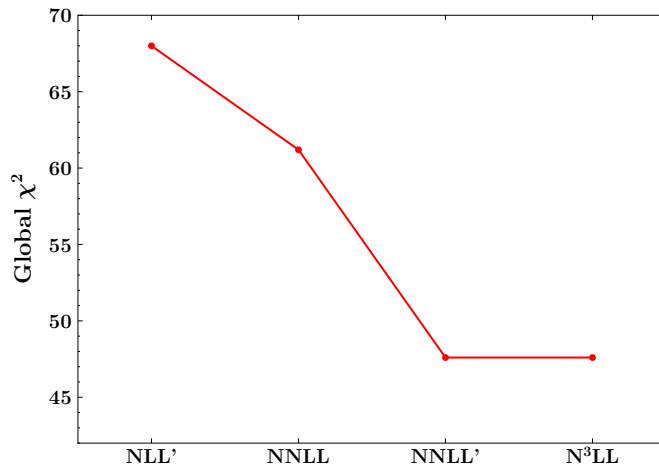


FIG. 4: Values of the global χ^2 of the fits at NLL', NNLL, NNLL' and N³LL perturbative accuracies.

We observe that the agreement between data and theory improves significantly moving from NLL' to NNLL', while it remains essentially unchanged taking a further step to N³LL. This indicates that the perturbative series is converging and that the inclusion of higher-order perturbative corrections is important to achieve an accurate description of data. We conclude that, given the current experimental uncertainties, NNLL' accuracy or higher is appropriate to reliably extract gluon TMDs.

In order to better visualise the impact of higher-order correction, in Fig. 5 we compare fitted theoretical predictions for all of the available perturbative orders to the ATLAS Run II ($H \rightarrow \gamma\gamma$) dataset. We see that the agreement between data and theory improves as the perturbative accuracy increases, with the NNLL' and N³LL predictions being able to reproduce at best both shape and normalisation of the dataset. In particular, the inclusion of higher-order corrections helps describe the peak and the tail of the distribution at relatively large values of q_T , which is the region where most of the tension between data and theory is observed at lower perturbative orders.

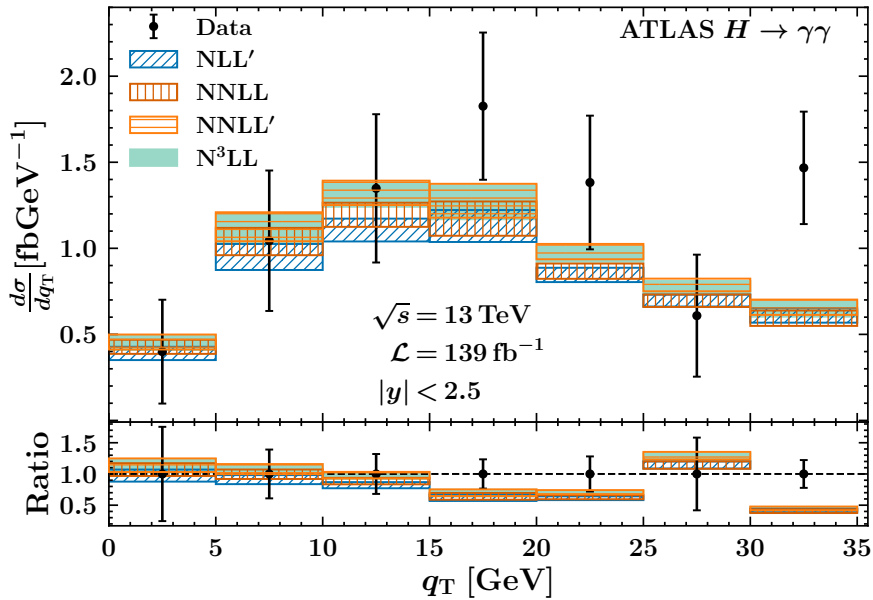


FIG. 5: Comparison between experimental data for the ATLAS Run II measurements at 13 TeV and the theoretical predictions obtained from the fits at NLL', NNLL, NNLL', and N³LL. The layout of the plot is the same as in Fig. 2.

D. Dependence on the q_T cut

Finally, in this section we discuss the dependence on the cut on the measured transverse momentum q_T . This is a key ingredient of any TMD fit since it restricts the analysis to the region where TMD factorisation is valid. In our baseline analysis, we include all data points with $q_T/M_H < 0.3$. Given the scarcity of Higgs data, this choice has the scope of retaining as much experimental information as possible while staying in the applicability region of TMD factorisation. Nonetheless, it is instructive to explore the effect of imposing more conservative cuts. In Tab. V, we report the values of the global χ^2/N_{dat} of the N³LL fit with the corresponding extracted value of the parameter g_1 for three different choice of the cut, namely $q_T/M_H < 0.2$, 0.25 , and the baseline cut 0.3 . We observe that the

Cut	N_{dat}	χ^2/N_{dat}	$g_1 [\text{GeV}^2]$
$q_T/M_H < 0.2$	20	1.08	7.1 ± 4.3
$q_T/M_H < 0.25$	28	1.35	12.6 ± 4.7
$q_T/M_H < 0.3$	30	1.49	14.4 ± 5.1

TABLE V: Values of the global χ^2/N_{dat} and extracted g_1 parameter of the fits at N³LL for different choices of the cut on q_T/M_H . The number of data points N_{dat} included in each fit is also reported.

data/theory agreement increases for more conservative cuts. In particular, the global χ^2/N_{dat} decreases from 1.49 for the baseline cut to 1.08 for the most conservative cut. This is an indication that some of the tension observed in the fit with the baseline cut can be attributed to data points in the region of relatively large q_T . However, the price to pay is a significant reduction of the number of data points, from 30 to 20, which also hampers a sound statistical interpretation of the results.

In order to better understand the origin of this tension, in Fig. 6 we compare the fitted theoretical predictions for the three different cuts to the ATLAS Run II ($H \rightarrow \gamma\gamma$) and CMS Run II combined datasets. We observe that the tension between data and theory is mostly driven by statistical fluctuations in the tail of the distribution at relatively large q_T . The tension is particularly evident for the CMS Run II combined dataset, which is the one with the largest χ^2/N_{dat} in Tab. IV. Indeed, the χ^2/N_{dat} for this dataset decreases from 4.46 for the baseline cut to 0.76 for the most conservative cut. For the data points included in all three cases, the agreement between data and theory is similar, which indicates that our choice of the baseline cut is not significantly biasing the TMD.

In the last column of Tab. V, we report the value of the extracted g_1 parameter for the three different cuts. We observe that the value of g_1 decreases for more conservative cuts, which is an indication that the data points in the region of relatively large q_T are driving the fit towards larger values of g_1 . However, given the current experimental

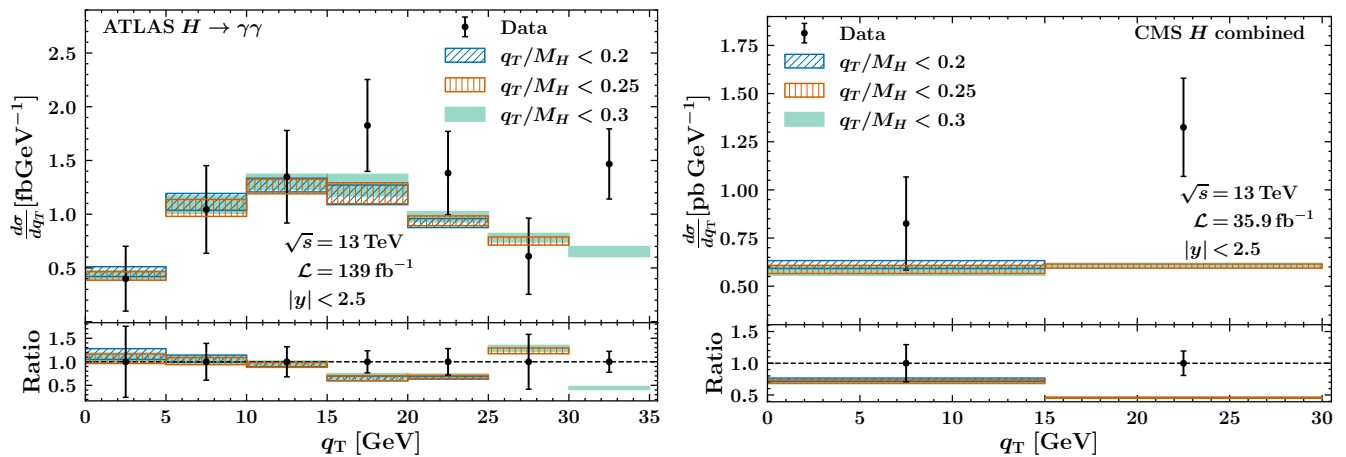


FIG. 6: Comparison between experimental data for the ATLAS Run II (left panel) and CMS Run II combined (right panel) measurements at 13 TeV and the theoretical predictions obtained from the fits with different cuts on q_T/M_H . The layout of the plot is the same as in Fig. 2.

uncertainties, the values of g_1 obtained with different cuts are compatible within one-sigma error. This is yet another indication that the choice of the baseline cut is not significantly affecting the fit results.

In order to better visualise the effect of the different cuts, in Fig. 7 we compare the gluon TMD at $\mu = \sqrt{\zeta} = M_H$ and $x = 0.01$ obtained from the fits with different cuts on q_T . As expected, distributions obtained with different cuts

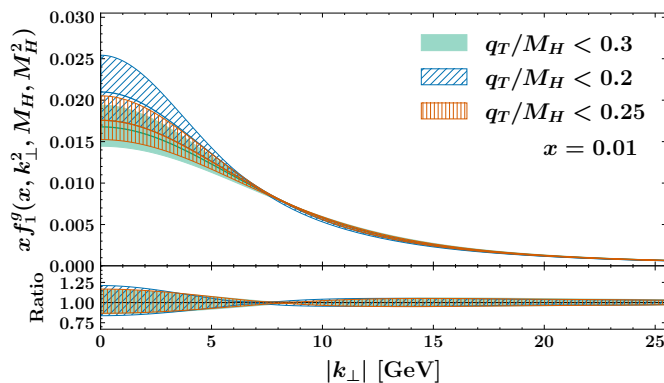


FIG. 7: The TMD PDF of the gluon in a proton at $\mu = \sqrt{\zeta} = M_H$ and $x = 0.01$ as a function of the partonic transverse momentum $|k_\perp|$ obtained from the fits with different cuts on q_T/M_H . Uncertainty bands correspond to one-sigma error.

are compatible within one-sigma error. We also see that the TMD obtained with the most conservative cut is slightly less broad than the one obtained with the baseline cut, which is consequence of the decrease of the g_1 . This is an indication that the data points in the region of relatively large q_T are driving the fit towards smaller TMDs at low $|k_\perp|$. However, given the current experimental uncertainties, this effect is not statistically significant.

V. CONCLUSION

In this work, we have presented the first extraction of the unpolarised gluon TMD f_1^g from LHC measurements of the Higgs-boson transverse-momentum distribution. The analysis is based on the complete set of available ATLAS and CMS data at $\sqrt{s} = 8$ and 13 TeV in the diphoton and four-lepton decay channels, and is carried out within the TMD factorisation framework at $N^3\text{LL}$ accuracy, including the linearly polarised gluon TMD $h_1^{\perp g}$ with its NNLO matching coefficient. The fit is implemented in the NangaParbat framework of the MAP Collaboration, and fiducial selections are consistently incorporated through a phase-space reduction factor computed for the relevant decay topologies.

The baseline fit, performed with the cut $q_T/M_H < 0.3$, reproduces both the shape and the normalisation of the experimental data with a global $\chi^2/N_{\text{dat}} = 1.49$, and yields an intrinsic nonperturbative parameter $g_1 = 14.4 \pm 5.1 \text{ GeV}^2$.

The relative uncertainty of about 35% reflects the limited sensitivity of current Higgs data to the nonperturbative content of gluon TMDs, a direct consequence of the large hard scale M_H at which the perturbative contribution dominates. The narrow-width approximation, together with the single scale spanned by the dataset, prevents us from separately constraining the nonperturbative component of the Collins-Soper kernel; the latter has therefore been estimated by rescaling the corresponding quark coefficient extracted in Ref. [50] by C_A/C_F . The study of perturbative convergence shows a marked improvement of the data/theory agreement from NLL' to NNLL' , and only mild changes when moving from NNLL' to N^3LL , indicating that the perturbative series has effectively stabilised at the highest accuracy considered. Variations of the q_T cut have a moderate impact on the extracted distribution: all values of g_1 obtained with different cuts are mutually compatible within one-sigma uncertainties, suggesting that the baseline choice does not introduce a significant bias in the extracted TMD.

Several directions naturally follow from this analysis. First, the inclusion of gluon-sensitive observables, possibly measured at future fixed-target experiments [51, 52], at scales significantly different from M_H . One such example is J/ψ -pair or other quarkonium production, which would enable a direct determination of the nonperturbative Collins-Soper kernel for gluons and disentangle the intrinsic component from the evolution contribution. Second, the increased statistical precision expected from Run III and the high-luminosity LHC programme should substantially tighten the determination of the nonperturbative parameters and eventually provide access to the x dependence of gluon TMDs, which is presently driven entirely by the perturbative matching onto collinear PDFs. Third, more flexible parametrisations of f_{NP} , possibly distinguishing between f_1^g and $h_1^{\perp g}$ and incorporating an explicit x dependence, will become meaningful as the data sample grows. We leave these developments to future work.

Acknowledgments

We would like to thank C. Pisano for helpful suggestions regarding the manuscript, N. Berger and P. Bortignon for insights on fiducial acceptance factors in ATLAS and CMS data. Initial stages of this work were performed during the ‘‘Hadron Physics 2030’’ program at the Institut Pascal (Universit  Paris-Saclay) with the support of the program ‘‘Investissements d’avenir’’ ANR-11-IDEX-0003-01. The work of S.A. and G.B. is supported by Fondazione di Sardegna through the project ‘‘Journey to the center of the proton’’, No. F23C25000150007. The work of V.B. has been supported by l’Agence Nationale de la Recherche (ANR), project ANR-24-CE31-7061-01.

Appendix A: Phase-space reduction factor

In this appendix we sketch the computation of the phase-space reduction factor \mathcal{P} introduced in Eq. (4), which encodes the effect of the kinematic cuts applied to the particles in the final state. The factor \mathcal{P} accounts for the impact of fiducial selections on the theoretical cross section. It is defined, for a generic N -particle final state, as the ratio of the squared decay amplitude integrated over the fiducial region to the same quantity integrated over the full phase space, namely

$$\mathcal{P}(q) = \frac{\int_{\text{fid. reg.}} d\Phi_N |\mathcal{M}(p_1, \dots, p_N)|^2}{\int d\Phi_N |\mathcal{M}(p_1, \dots, p_N)|^2}, \quad (\text{A1})$$

where q is the four-momentum of the decaying particle, \mathcal{M} is the amplitude of the decay process and $d\Phi_N$ is the N -body Lorentz-invariant phase space,²

$$d\Phi_N(q; p_1, \dots, p_N) = (2\pi)^4 \delta^{(4)}\left(q - \sum_{i=1}^N p_i\right) \prod_{i=1}^N \frac{d^4 p_i}{(2\pi)^3} \delta(p_i^2) \theta(p_{i,0}). \quad (\text{A2})$$

In the following, we discuss the computation of \mathcal{P} for the two-body and four-body final states relevant to the diphoton and four-lepton decay channels of the Higgs boson, respectively. We first treat the diphoton channel, $H \rightarrow \gamma\gamma$ and then we extend the construction to the four-lepton channel, $H \rightarrow 4\ell$.

² Throughout this appendix we neglect the mass of the final-state particles, so that the on-shell condition reduces to $p_i^2 = 0$.

1. Cuts on the two-particle final state

For the diphoton final state, Eq. (A1) reads

$$\mathcal{P}(q) = \frac{\int_{\text{fid. reg.}} d^4 p_1 d^4 p_2 \delta(p_1^2) \delta(p_2^2) \theta(p_{1,0}) \theta(p_{2,0}) \delta^{(4)}(p_1 + p_2 - q) |\mathcal{M}(p_1, p_2)|^2}{\int d^4 p_1 d^4 p_2 \delta(p_1^2) \delta(p_2^2) \theta(p_{1,0}) \theta(p_{2,0}) \delta^{(4)}(p_1 + p_2 - q) |\mathcal{M}(p_1, p_2)|^2}, \quad (\text{A3})$$

where p_1 and p_2 are the four-momenta of the outgoing photons, $q = p_1 + p_2$, and $\mathcal{M}(p_1, p_2)$ is the amplitude for the decay $H \rightarrow \gamma\gamma$. This latter can be written as

$$\mathcal{M} = \frac{e^2 g}{(4\pi)^2 M_W} F(p_1 \cdot p_2 g^{\mu\nu} - p_2^\mu p_1^\nu) \epsilon_\mu(p_1) \epsilon_\nu(p_2), \quad (\text{A4})$$

where e is the electromagnetic coupling, g is the weak coupling, M_W is the W -boson mass and $\epsilon_\mu(p_i)$ is the photon polarisation vector. The function F collects the contributions of W and fermion loops,

$$F = F_W(\beta_W) + \sum_f N_c Q_f^2 F_f(\beta_f), \quad (\text{A5})$$

with $N_c = 1$ for leptons and $N_c = 3$ for quarks, and

$$\beta_W = \frac{4M_W^2}{M_H^2}, \quad \beta_f = \frac{4m_f^2}{M_H^2}, \quad (\text{A6})$$

while

$$\begin{aligned} F_W(\beta) &= 2 + 3\beta + 3\beta(2 - \beta) f(\beta), \\ F_f(\beta) &= -2\beta [1 + (1 - \beta) f(\beta)], \end{aligned} \quad (\text{A7})$$

with $f(\beta)$ the function defined in Eq. (3). Summing over photon polarisations, one obtains

$$|\mathcal{M}|^2 \propto F^2 \frac{(p_1 + p_2)^4}{2}, \quad (\text{A8})$$

so that Eq. (A3) becomes

$$\mathcal{P}(q) = \frac{\int_{\text{fid. reg.}} d^4 p_1 d^4 p_2 \delta(p_1^2) \delta(p_2^2) \theta(p_{1,0}) \theta(p_{2,0}) \delta^{(4)}(p_1 + p_2 - q) (p_1 + p_2)^4}{\int d^4 p_1 d^4 p_2 \delta(p_1^2) \delta(p_2^2) \theta(p_{1,0}) \theta(p_{2,0}) \delta^{(4)}(p_1 + p_2 - q) (p_1 + p_2)^4}. \quad (\text{A9})$$

The restriction of the integration domain to the fiducial region can be implemented through a generalised step function $\Theta(p_1, p_2)$, which equals one inside the fiducial region and vanishes outside. This allows one to extend the numerator integration to the full two-photon phase space. Exploiting momentum conservation through the four-dimensional δ -function both in the numerator and in the denominator, and dropping the overall factor $(p_1 + p_2)^4 = q^4$, which is independent of the integration variables, the phase-space reduction factor takes the compact form

$$\mathcal{P}(q) = \frac{\int d^4 p \delta(p^2) \delta((q - p)^2) \theta(p_0) \theta(q_0 - p_0) \Theta(p, q - p)}{\int d^4 p \delta(p^2) \delta((q - p)^2) \theta(p_0) \theta(q_0 - p_0)}. \quad (\text{A10})$$

The two outgoing photons are subject to asymmetric, hierarchy-dependent selections, as summarised in Table III. Following the standard experimental convention, the leading (subleading) photon is defined as the one with the largest (smallest) transverse momentum, and a different p_T threshold is applied accordingly. Because of asymmetric cuts on the photon rapidities, see Table III, an analytic evaluation of Eq. (A10) is not feasible, and we rely on a Monte Carlo integration.

2. Cuts on the four-particle final state

We now extend the calculation of the phase-space reduction factor \mathcal{P} to the four-lepton final state,

$$\mathcal{P}(q) = \frac{\int_{\text{fid. reg.}} d\Phi_4 |\mathcal{M}(p_1, p_2, p_3, p_4)|^2}{\int d\Phi_4 |\mathcal{M}(p_1, p_2, p_3, p_4)|^2}, \quad (\text{A11})$$

where p_i ($i = 1, \dots, 4$) are the lepton four-momenta, \mathcal{M} is the amplitude for the decay $H \rightarrow ZZ \rightarrow 4\ell$, and $d\Phi_4$ is the four-body Lorentz-invariant phase space defined according to Eq. (A2). The decay amplitude can be written in terms of the HZZ vertex, the two Z propagators, and the leptonic currents. Recalling the Z -boson couplings to fermions,

$$g_Z = \frac{e}{\sin\theta_W \cos\theta_W}, \quad v_f = I_{3,f} - 2Q_f \sin^2\theta_W, \quad a_f = I_{3,f}, \quad (\text{A12})$$

with θ_W the weak mixing angle, $I_{3,f}$ the third component of the weak isospin of the fermion f , and Q_f its electric charge (for charged leptons $I_{3,\ell} = -\frac{1}{2}$ and $Q_\ell = -1$), the amplitude reads

$$\begin{aligned} \mathcal{M} = & i g_Z M_Z g_{\mu\nu} \left\{ \frac{-i g^{\mu\lambda}}{(p_1 + p_2)^2 - M_Z^2 + i\Gamma_Z M_Z} \frac{-i g_Z}{2} \bar{u}_e^{s_1}(p_1) \gamma_\lambda (v_\ell - a_\ell \gamma_5) v_e^{s_2}(p_2) \right\} \\ & \times \left\{ \frac{-i g^{\nu\rho}}{(p_3 + p_4)^2 - M_Z^2 + i\Gamma_Z M_Z} \frac{-i g_Z}{2} \bar{u}_\mu^{s_3}(p_3) \gamma_\rho (v_\ell - a_\ell \gamma_5) v_\mu^{s_4}(p_4) \right\}, \end{aligned} \quad (\text{A13})$$

where M_Z and Γ_Z are mass and width of the Z boson, and s_i are the lepton spin indices. After summing over the lepton spins, the squared amplitude takes the form

$$|\mathcal{M}|^2 \propto \frac{[(v_\ell^2 + a_\ell^2)^2 + 4v_\ell^2 a_\ell^2] (p_1 \cdot p_3)(p_2 \cdot p_4) + (v_\ell^2 - a_\ell^2)^2 (p_1 \cdot p_4)(p_2 \cdot p_3)}{[(p_1 + p_2)^2 - M_Z^2]^2 + \Gamma_Z^2 M_Z^2 [(p_3 + p_4)^2 - M_Z^2]^2 + \Gamma_Z^2 M_Z^2}. \quad (\text{A14})$$

The explicit dependence on the individual lepton momenta in Eq. (A14) prevents any further analytic reduction of Eq. (A11), and a numerical evaluation is required.

To enable an efficient numerical evaluation and a transparent implementation of the fiducial cuts, we factorise the four-body phase space into a sequence of nested two-body phase spaces, in accordance with the tree-level topology of the decay $H \rightarrow ZZ \rightarrow 4\ell$. We introduce the intermediate four-momenta

$$q_1 = p_1 + p_2, \quad q_2 = p_3 + p_4, \quad q_1 + q_2 = q, \quad (\text{A15})$$

together with their virtualities $Q_1^2 \equiv q_1^2$ and $Q_2^2 \equiv q_2^2$. Inserting two unit factors of the form $\int dQ_i^2 \delta(q_i^2 - Q_i^2)$ into Eq. (A2), the four-body phase space factorises as

$$d\Phi_4(q; p_1, p_2, p_3, p_4) = \frac{dQ_1^2 dQ_2^2}{(2\pi)^2} d\Phi_2(q; q_1, q_2) d\Phi_2(q_1; p_1, p_2) d\Phi_2(q_2; p_3, p_4). \quad (\text{A16})$$

This decomposition is particularly well suited for a Monte Carlo implementation: each two-body sub-phase space is parametrised by two angular variables in the corresponding rest frame, while the virtualities Q_1^2 and Q_2^2 are sampled independently with an importance-sampling weight tuned on the two Z Breit-Wigner peaks of Eq. (A14). This procedure reduces the effective dimensionality of the integration while exposing simple two-body kinematics, and allows the fiducial selections of Table II (p_T thresholds, $|\eta|$ windows, m_{Z_1}/m_{Z_2} mass windows, ordered-lepton cuts) to be imposed directly at particle level. Eq (A11) can thus be evaluated numerically in a stable and efficient way for any value of the kinematic variables (Q, y, q_T) .

-
- [1] J. C. Collins, D. E. Soper, and G. F. Sterman, Nucl. Phys. B **250**, 199 (1985).
- [2] J. Collins, *Foundations of Perturbative QCD*, vol. 32 (Cambridge University Press, 2011), ISBN 978-1-009-40184-5, 978-1-009-40183-8, 978-1-009-40182-1.
- [3] A. Bacchetta, F. Delcarro, C. Pisano, M. Radici, and A. Signori, JHEP **06**, 081 (2017), [Erratum: JHEP 06, 051 (2019)], 1703.10157.
- [4] V. Bertone, I. Scimemi, and A. Vladimirov, JHEP **06**, 028 (2019), 1902.08474.
- [5] I. Scimemi and A. Vladimirov, JHEP **06**, 137 (2020), 1912.06532.
- [6] A. Bacchetta, V. Bertone, C. Bissolotti, G. Bozzi, F. Delcarro, F. Piacenza, and M. Radici, JHEP **07**, 117 (2020), 1912.07550.
- [7] A. Bacchetta, V. Bertone, C. Bissolotti, G. Bozzi, M. Cerutti, F. Piacenza, M. Radici, and A. Signori (MAP (Multi-dimensional Analyses of Partonic distributions)), JHEP **10**, 127 (2022), 2206.07598.
- [8] M. Bury, F. Hautmann, S. Leal-Gomez, I. Scimemi, A. Vladimirov, and P. Zurita, JHEP **10**, 118 (2022), 2201.07114.
- [9] V. Moos, I. Scimemi, A. Vladimirov, and P. Zurita, JHEP **05**, 036 (2024), 2305.07473.
- [10] A. Bacchetta, V. Bertone, C. Bissolotti, G. Bozzi, M. Cerutti, F. Delcarro, M. Radici, L. Rossi, and A. Signori (MAP (Multi-dimensional Analyses of Partonic distributions)), JHEP **08**, 232 (2024), 2405.13833.
- [11] V. Moos, I. Scimemi, A. Vladimirov, and P. Zurita, JHEP **11**, 134 (2025), 2503.11201.
- [12] A. Bacchetta, V. Bertone, C. Bissolotti, M. Cerutti, M. Radici, S. Rodini, and L. Rossi (MAP (Multi-dimensional Analyses of Partonic distributions)), Phys. Rev. Lett. **135**, 021904 (2025), 2502.04166.
- [13] S. Catani and M. Grazzini, Nucl. Phys. B **570**, 287 (2000), hep-ph/9908523.
- [14] S. Catani, D. de Florian, and M. Grazzini, Nucl. Phys. B **596**, 299 (2001), hep-ph/0008184.
- [15] G. Bozzi, S. Catani, D. de Florian, and M. Grazzini, Nucl. Phys. B **737**, 73 (2006), hep-ph/0508068.
- [16] F. Scarpa, D. Boer, M. G. Echevarria, J.-P. Lansberg, C. Pisano, and M. Schlegel, Eur. Phys. J. C **80**, 87 (2020), 1909.05769.
- [17] J.-P. Lansberg, C. Pisano, F. Scarpa, and M. Schlegel, Phys. Lett. B **784**, 217 (2018), [Erratum: Phys.Lett.B 791, 420–421 (2019)], 1710.01684.
- [18] P. Sun, B.-W. Xiao, and F. Yuan, Phys. Rev. D **84**, 094005 (2011), 1109.1354.
- [19] D. Boer, W. J. den Dunnen, C. Pisano, M. Schlegel, and W. Vogelsang, Phys. Rev. Lett. **108**, 032002 (2012), 1109.1444.
- [20] D. Boer, W. J. den Dunnen, C. Pisano, and M. Schlegel, Phys. Rev. Lett. **111**, 032002 (2013), 1304.2654.
- [21] D. Boer and C. Pisano, Phys. Rev. D **91**, 074024 (2015), 1412.5556.
- [22] D. Boer and W. J. den Dunnen, Nucl. Phys. B **886**, 421 (2014), 1404.6753.
- [23] A. Bacchetta, F. G. Celiberto, M. Radici, and P. Taels, Eur. Phys. J. C **80**, 733 (2020), 2005.02288.
- [24] A. Bacchetta, F. G. Celiberto, and M. Radici, Eur. Phys. J. C **84**, 576 (2024), 2402.17556.
- [25] R. P. Kauffman, Phys. Rev. D **44**, 1415 (1991).
- [26] C. P. Yuan, Phys. Lett. B **283**, 395 (1992).
- [27] W. Bizoń, X. Chen, A. Gehrmann-De Ridder, T. Gehrmann, N. Glover, A. Huss, P. F. Monni, E. Re, L. Rottoli, and P. Torrielli, JHEP **12**, 132 (2018), 1805.05916.
- [28] G. Billis, B. Dehnadi, M. A. Ebert, J. K. L. Michel, and F. J. Tackmann, Phys. Rev. Lett. **127**, 072001 (2021), 2102.08039.
- [29] P. J. Mulders and J. Rodrigues, Phys. Rev. D **63**, 094021 (2001), hep-ph/0009343.
- [30] S. Catani and M. Grazzini, Nucl. Phys. B **845**, 297 (2011), 1011.3918.
- [31] T. Becher, M. Neubert, and D. Wilhelm, JHEP **05**, 110 (2013), 1212.2621.
- [32] D. Gutierrez-Reyes, S. Leal-Gomez, I. Scimemi, and A. Vladimirov, JHEP **11**, 121 (2019), 1907.03780.
- [33] R. K. Ellis, W. J. Stirling, and B. R. Webber, *QCD and collider physics*, vol. 8 (Cambridge University Press, 2011), ISBN 978-0-511-82328-2, 978-0-521-54589-1.
- [34] R. D. Ball et al. (NNPDF), Eur. Phys. J. C **77**, 663 (2017), 1706.00428.
- [35] A. Buckley, J. Ferrando, S. Lloyd, K. Nordström, B. Page, M. Rüfenacht, M. Schönherr, and G. Watt, Eur. Phys. J. C **75**, 132 (2015), 1412.7420.
- [36] M. Cerutti and A. Simonelli (2026), 2603.19088.
- [37] A. Tumasyan et al. (CMS), JHEP **07**, 091 (2023), 2208.12279.
- [38] A. Hayrapetyan et al. (CMS), JHEP **08**, 040 (2023), 2305.07532.
- [39] A. M. Sirunyan et al. (CMS), Phys. Lett. B **792**, 369 (2019), 1812.06504.
- [40] V. Khachatryan et al. (CMS), Eur. Phys. J. C **76**, 13 (2016), 1508.07819.
- [41] G. Aad et al. (ATLAS), JHEP **08**, 027 (2022), 2202.00487.
- [42] G. Aad et al. (ATLAS), Eur. Phys. J. C **80**, 942 (2020), 2004.03969.
- [43] M. Aaboud et al. (ATLAS), Phys. Lett. B **786**, 114 (2018), 1805.10197.
- [44] G. Aad et al. (ATLAS), JHEP **09**, 112 (2014), 1407.4222.
- [45] G. Aad et al. (ATLAS), Phys. Lett. B **738**, 234 (2014), 1408.3226.
- [46] M. Cerutti, L. Rossi, S. Venturini, A. Bacchetta, V. Bertone, C. Bissolotti, and M. Radici (MAP (Multi-dimensional Analyses of Partonic distributions)), Phys. Rev. D **107**, 014014 (2023), 2210.01733.
- [47] A. Bacchetta, A. Bongallino, M. Cerutti, M. Radici, and L. Rossi (MAP (Multi-dimensional Analyses of Partonic distributions)), Phys. Rev. Lett. **134**, 121901 (2025), 2409.18078.
- [48] L. Rossi, A. Bacchetta, M. Cerutti, and M. Radici (MAP (Multi-dimensional Analyses of Partonic distributions)) (2025), 2509.25098.

- [49] S. Camarda, G. Ferrera, and L. Rossi, *JHEP* **01**, 150 (2026), 2508.06201.
- [50] A. Avkhadiev, V. Bertone, C. Bissolotti, M. Cerutti, Y. Fu, S. Rodini, P. Shanahan, M. Wagman, and Y. Zhao, *Phys. Rev. Lett.* **136**, 171902 (2026), 2510.26489.
- [51] C. Hadjidakis et al., *Phys. Rept.* **911**, 1 (2021), 1807.00603.
- [52] C. A. Aidala et al. (2019), 1901.08002.